Journal of the European Ceramic Society xxx (xxxx) xxx–xxx

Contents lists available at ScienceDirect

Journal of the European Ceramic Society

journal homepage: www.elsevier.com/locate/jeurceramsoc

Original Article

Significant enhancement of the thermoelectric performance in $Ca_3Co_4O_9$ thermoelectric materials through combined strontium substitution and hot-pressing process

M.A. Torres[a], F.M. Costa[b], D. Flahaut[c], K. Touati[d], Sh. Rasekh[b,e], N.M. Ferreira[b,e], J. Allouche[c], M. Depriester[d], M.A. Madre[a], A.V. Kovalevsky[e], J.C. Diez[a], A. Sotelo[a,*]

[a] ICMA (CSIC-Universidad de Zaragoza), C/María de Luna 3, 50018 Zaragoza, Spain
[b] i3N, Departamento de Física, Universidade de Aveiro, 3810-193 Aveiro, Portugal
[c] CNRS/Univ. Pau & Pays de l'Adour, Institut des Sciences Analytiques et de Physico-chimie pour l'Environnement et les Matériaux, UMR5254, 64000 Pau, France
[d] UDSMM (EA 4476), MREI-1, Université du Littoral Côte d'Opale, 59140 Dunkerque, France
[e] CICECO – Aveiro Institute of Materials, Department of Materials and Ceramic Engineering, University of Aveiro, 3810-193 Aveiro, Portugal

ARTICLE INFO

Keywords:
Ceramics
Oxides
Hot-pressing
Texture
Electrical properties

ABSTRACT

This work explores the possibilities for a further enhancement of the thermoelectric properties of $Ca_3Co_4O_9$ by Sr-doping combined with hot-pressing. Modified hot-pressing process resulted in highly-textured and dense ceramics. Sr-doping significantly improves electrical properties, resulting in extremely large power factor (1.2 mW/K^{2}m at 800 °C) due to simultaneous electrical resistivity decrease and Seebeck coefficient increase. The main effect on cumulative electrical performance is provided by the Seebeck coefficient, reaching 270μV/K at 800 °C. XPS revealed relatively high average cobalt oxidation state at room temperature (+3.3), compared to materials produced by conventional sintering. The results of combined XPS and Auger electron spectroscopy emphasize the importance of high densification in $Ca_3Co_4O_9$-based ceramics for preventing phase decomposition and interaction with CO_2 and moisture. Still, despite the exceptional electrical performance, the calculated figure-of-merit (estimated as 0.29 at 800 °C) is around the best reported in the literature due to a high thermal conductivity (4.4 W/K m at room temperature).

1. Introduction

Thermoelectric (TE) materials are characterized by their ability to directly convert heat into electrical energy due to the Seebeck coefficient (thermoelectric effect). The thermoelectric efficiency is generally determined by the temperature gradient and the dimensionless figure of merit, ZT, related to the basic material properties, and defined as $TS^2/\rho\kappa$, where S is Seebeck coefficient, ρ, electrical resistivity, κ, thermal conductivity, and T is the absolute temperature [1]. In the current climate change scenario, thermoelectricity has attracted much attention as a solution to improve the efficiency of the classical energy conversion systems by harvesting the waste heat [2]. Consequently, this technology will help fighting against climate change by decreasing the fossil fuels consumption and reducing the amount of released CO_2. Very promising directions include solar thermoelectric generators [3], or heating/refrigeration devices [4]. Nowadays, these commercial applications involve intermetallic thermoelectric materials, such as Bi_2Te_3 or $CoSb_3$, with high TE performances at relatively low temperatures [5,6]. However, they degrade even at moderately high temperatures under air atmosphere and/or release toxic or heavy elements. Higher operation temperatures are favorable in terms of increasing Carnot efficiency. The discovery of attractive thermoelectric properties in $Na_2Co_2O_4$ [7], suggested oxides could be a suitable alternative to traditional thermoelectrics, enabling energy harvesting at elevated temperatures. Therefore, these materials have been deeply studied [8–10], since, besides reasonable TE performance, they can operate at high temperatures in air without degradation.

The anisotropy of these cobaltite-based materials [11] has been exploited by preferentially aligning their grains to enhance electrical conductivity. On the other hand, the decrease of electrical resistivity is usually accompanied with a decrease in S and an increase in κ values, as they are linked to each other. Due to these correlations, ZT improvement is a very difficult task. Several approaches have to be simultaneously used to maximize ZT in $Ca_3Co_4O_9$ as, for example, texturing

* Corresponding author.
E-mail address: asotelo@unizar.es (A. Sotelo).

https://doi.org/10.1016/j.jeurceramsoc.2018.12.049
Received 29 August 2018; Received in revised form 20 December 2018; Accepted 21 December 2018

and doping. Among texturing techniques, it is important to highlight the spark plasma sintering (SPS) [12,13], sinter-forging [14], template grain growth (TGG) [15], laser floating zone (LFZ) [16], and the electrically-assisted laser floating zone method (EALFZ) [17]. When considering doping processes, alio- and isovalent substitutions (i.e. Yb^{3+} for Ca^{2+}, and Sr^{2+} for Ca^{2+}, respectively) [18,19] can be performed. In the first situation, Yb modifies the rock-salt layer size (raising ρ and S) and charge (decreasing the Co^{4+} proportion, increasing S and ρ). Moreover, its high atomic mass enhances phonon scattering, leading to lower thermal conductivity [20]. This is a more complex situation than in isovalent substitution, where only modifications in the rock-salt layer dimensions, and effects on the phonon scattering, are present.

This work aims at producing high-density textured undoped and Sr-doped $Ca_3Co_4O_9$ ceramic materials, with expected enhancement of TE properties induced by doping and texturing processes. Based on previously published results [21–24], samples were prepared through the classical solid state method, and textured using the hot-uniaxial pressing technique. The structural and microstructural features of these samples were studied and correlated with the thermoelectric properties.

2. Experimental

2.1. Samples preparation

Initial $Ca_3Co_4O_9$ and $Ca_{2.93}Sr_{0.07}Co_4O_9$ ceramic precursors were prepared from commercial $CaCO_3$ (≥ 99%, Aldrich), $SrCO_3$ (≥ 98%, Aldrich), and CoO (99.99%, Aldrich) powders using the classical solid state method [25]. After calcining procedure, the pre-reacted powders were cold uniaxially pressed at 300 MPa in form of disks (25 mm diameter and 5 mm thick) and sintered at 900 °C for 24 h, under air, with a final furnace cooling. The sintered disks were uniaxially hot-pressed at 25 MPa (900 °C 12 h), under air, with a final furnace cooling. For this process, these disks were placed between two Ag foils, and two alumina blocks. Finally, the samples were cut into pieces for their structural and thermoelectric characterization.

2.2. Structural and microstructural characterization

Phase identification was performed by powder X-ray diffraction (XRD) using a PANalytical X'Pert MPD Philips diffractometer (CuK_α radiation, λ = 1.54056 Å) at 40 kV and 30 mA, with a step 0.02° in 1 s, and 2θ angle ranging 10–60°. Phase indexation was made using the JCPDS database. Texture analysis (pole figure) to quantify the grain alignment degree, was performed for all samples in a diffractometer Philips MRD using the diffraction peak at 37.1 °, corresponding to the ($\bar{2}$ 010) crystallographic plane.

Microstructural characterization was performed on longitudinal surfaces and transversal fractures of samples using a Field Emission Scanning Electron Microscope (FESEM, Zeiss Merlin) equipped with an energy dispersive spectrometry (EDS) analysis system. In order to obtain more guidelines on the morphology and microstructural features, surface sections were polished and chemically etched in HCl (6 M) for 2 s. Apparent density measurements have been performed after each processing step to obtain preliminary information on the microstructural evolution in the samples.

High-resolution SEM images in secondary emission mode, used as references for AES analysis, were obtained using the same equipment operating in SEM mode (30 keV, 2 nA, working distance = 23 mm).

2.3. XPS and AES characterization

The surface atomic composition and chemical environment of elements at the surface were determined using X-ray photoelectron spectroscopy (XPS) analysis, following the procedure described in previous works [26].

Before AES analyses, samples were cross-cut with a JEOL Cross-Polisher (JEOL Ltd.), using ion-milling polishing method. A stainless steel shield plate was used to protect one-half of the sample, while the non-protected area was etched with an Ar^+-ion beam (6 keV). After cutting, the samples were mounted on a sample holder for Auger analyses, as previously reported [26].

2.4. Thermoelectric characterization

Electrical resistivity and Seebeck coefficient were simultaneously measured by the standard four-probe DC technique in a LSR-3 system (Linseis GmbH). The samples were measured in the steady state mode at temperatures ranging from 50 to 800 °C under He atmosphere. Thermal conductivity was determined, in the same direction with the Seebeck and electrical resistivity measurements, using the photothermal radiometry technique (PTR) under air atmosphere [27], following the procedure described in [28]. ZT values were calculated at 25–160 °C, using power factor ($PF = S^2/\rho$) and κ data. In addition, they were estimated at higher temperatures, considering κ unchanged with temperature, and compared to the best up-to-date literature. Taking into account that the thermal conductivity of $Ca_3Co_4O_9$-based materials decreases on heating [29,30], real κ values are expected to be lower than the estimated ones, and actual TE performances at high temperatures can be notably higher.

3. Results and discussion

3.1. XRD characterization

XRD patterns, shown in Fig. 1, indicate that both samples possess similar phase composition. Major peaks correspond to the $Ca_3Co_4O_9$–based phase, in accordance with the incommensurate superstructure described in [31]. Despite noticeable peaks broadening, due to the microstructural effects described below, the peaks shift towards lower 2θ angles in Sr-doped samples indicates the Sr^{2+} substitution. On the other hand, some minor peaks corresponding to the $Ca_3Co_2O_6$ phase were also observed [32,33], in agreement with the available literature [19,34,35]. The most intense peaks are associated with (00l0) planes, likely provided with preferential orientation of grains due to their plate-like shape, in accordance with previous results [21]. Representative poles figure of $Ca_3Co_4O_9$ sample, shown in Fig. SI1, indicates significant and very similar grain alignment (around 13° misalignment), with their *ab*-planes parallel to the sample surface, pointing out to a negligible effect of Sr-doping on the grains orientation.

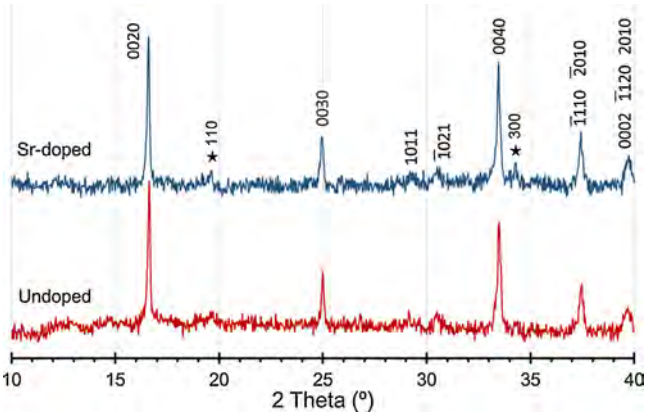

Fig. 1. Powder XRD patterns of undoped and Sr-doped $Ca_3Co_4O_9$ samples. Diffraction planes indicate the reflections corresponding to $Ca_3Co_4O_9$ phase, while * identify those associated to $Ca_3Co_2O_6$ one.

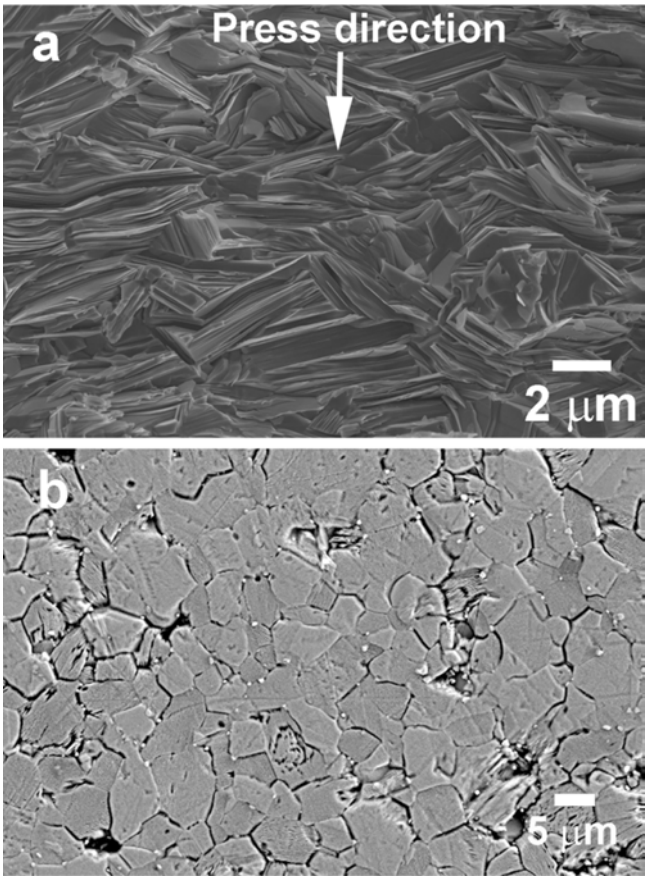

Fig. 2. Representative SEM micrographs taken on a) fractured transversal sections of $Ca_3Co_4O_9$ samples (The arrow indicates the pressure direction in the cold and the hot-uniaxial pressing processes); and b) polished surface of Sr-doped samples after chemical etching.

3.2. Microstructure

Fig. 2a shows a representative transversal fractured section of undoped samples after uniaxial hot-pressing process. In spite of the conventional sintering procedure preceding it, the plate-like grains show a relatively good orientation, in agreement with the pole figures results. Moreover, the grains show a significant aspect ratio, with grain sizes exceeding 5 μm along the *a*- and *b*-directions, being much smaller in the *c*-one.

Fig. 2b, shows a representative view of the polished surface of Sr-doped samples after etching. It suggests low porosity in these samples, while the big pores are likely due to the polishing procedure. Moreover, it confirms that grains are larger than 5 μm along the *a*- and *b*-directions. EDS analysis has shown that they are formed by single $Ca_3Co_4O_9$, and $Ca_{2.93}Sr_{0.07}Co_4O_9$ phases in the undoped and Sr-doped samples, respectively. On the other hand, no $Ca_3Co_2O_6$ phase has been detected, most likely due to its low amount, as observed in the powder XRD patterns. This indicates that the processing conditions are adequate to produce nearly single thermoelectric phase with highly oriented grains.

Density evolution after each processing step (pressing, sintering, and hot-pressing) was determined using 4.68 g/cm^3 as reference for the theoretical one [36]. The results displayed in Table 1 confirm the very low porosity of the hot-pressed samples. Moreover, both samples possess very close relative densities after each processing step. They slightly increase after sintering due to the relatively low temperatures, imposed by its stability limit (around 920 °C), while the minimum temperature to form liquid phase is ~1350 °C [37]. This limitation leads to densities lower than 80% in the available literature [38,39]. Therefore, highly-dense $Ca_3Co_4O_9$-based materials require other processes

Table 1
Relative density of samples after different processing steps.

	Relative density (%)		
	Pressed	Sintered	Hot-pressed
$Ca_3Co_4O_9$	62.0 ± 2.7	75.1 ± 1.3	95.1 ± 0.7
$Ca_{2.97}Sr_{0.03}Co_4O_9$	60.0 ± 2.1	74.2 ± 1.0	95.0 ± 0.5

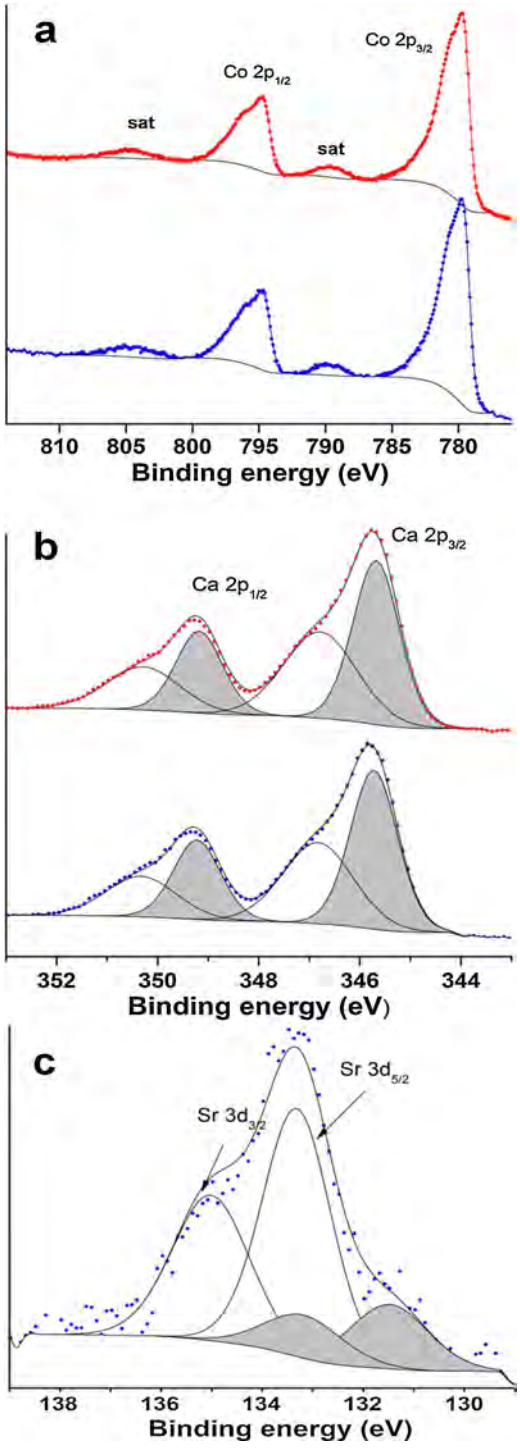

Fig. 3. XPS spectra obtained in undoped (-); and Sr-doped (-) $Ca_3Co_4O_9$ samples, for a) Co 2p; b) Ca 2p; and c) Sr 3d spectra in Sr-doped ones.

including two-step sintering [40], melt-solidification [41], SPS [42], or hot-pressing [14], to reach densities close to the theoretical one (see Table 1).

3.3. XPS and AES analysis

XPS spectra were recorded for Ca 2p, Co 2p, O 1 s, Sr 3d and C 1 s regions, corresponding to binding energies (B.E.) and atomic percentages shown in Table SI1.

Co 2p core peaks presented in Fig. 3a consist in two main components Co $2p_{3/2}$ and Co $2p_{1/2}$, at 780.3 and 794.8 eV, respectively, with satellite peaks at 789.6 and 804.7 eV. The satellite relative area of the main Co 2p peak allows determining the average Co oxidation state [43] as +3.3, higher than the obtained in sintered materials [25]. On the other hand, the shoulders at high-binding-energy are attributed to the interaction between CoO_6 clusters [44].

Ca 2p spectra (Fig. 3b) can be decomposed into two doublets associated to: i) calcium in the rock salt layer [45] (Ca-O, B.E. Ca $2p_{3/2}$ = 345.7 eV) and ii) calcium carbonate (B.E. (Ca $2p_{3/2}$) = 346.8 eV) [46].

In Sr-doped material, the overall shape of the Co 2p core peak is retained, and no evolution of the oxidation state has been detected. On the other hand, two chemical environments can be identified for Sr (Fig. 3c); i) Sr in carbonate environment (B.E. Sr $3d_{5/2}$ = 133.4 eV [47]), and ii) Sr^{2+} in the $Ca_{2.93}Sr_{0.07}Co_4O_9$ phase (B.E (Sr $3d_{5/2}$) = 131.5 eV). Thus, only a limited part of strontium (25% of the Sr 2p entire signal) seems to substitute Ca in the rock salt layer.

The composition obtained from XPS analyses is $Ca_{2.6 \pm 0.1}Co_4O_{8.1 \pm 0.1}$ for the undoped and $Ca_{2.9 \pm 0.1}Sr_{0.1 \pm 0.1}Co_4O_{8.7 \pm 0.1}$ for the Sr-doped materials, close to the determined through EDS analyses. The deviation of surface composition from the nominal one is usually reported in XPS quantitative analyses.

AES analysis was performed on both for undoped and Sr-doped samples. Two single point analyses were carried out on the undoped sample, within (dot 1) and outside (dot 2) a holed region (Fig. 4a). As it can be observed in Fig. 4b, Co LMM (320–703 eV) and O KLL (460–530 eV) transitions are clearly identifiable in both dots. In addition, overlapped transitions of Ca LMM and C KLL are also observed at 240–330 eV. Consequently, carbon transition could not be correctly extracted from the curve. However, it shows a higher peak intensity ratio between Ca/C and Co transitions within the holed region (dot 1). This is confirmed by AES chemical mapping (Fig. SI2) showing higher Ca and O, and lower Co signals within the porous region. These results are in good agreement with the presence of $CaCO_3$ environments, previously identified by XPS.

In the Sr-doped material, Sr rich inclusions have been identified by Auger spectroscopy. In Fig. 5a, SEM micrograph of a Sr-rich inclusion, together with the location of two target dots, are shown. The spectra of the two dots (Fig. 5b) show Ca, C and Co transitions within the same energy ranges found in the undoped material. Moreover, a Sr LMM transition at 1475–1660 eV for dot 1 is also identified. AES mapping (Fig. SI3) confirms that Sr is only detected within the inclusion whereas Co is detected outside (overlay Fig. SI3). This is due to the increased reactivity of Sr with moisture and CO_2 [48]; this can result in exsolution of Sr from the $Ca_3Co_4O_9$ phase, producing these large particles. Such interactions impose some limitations on the applicability of the XPS, but still some guidelines can be obtained from the results presented in Table SI1.

Both type of samples show a significant deviation from the nominal Ca(Sr):Co ratio (Sr/Co = 0.1; Ca/Co ˜ 1.2 from XPS analyses), suggesting a Ca(Sr) excess at the surface. This enrichment is mainly produced in the surface by forming carbonates, corroborating Auger spectroscopy results and explaining why they are not been detected on XRD patterns.

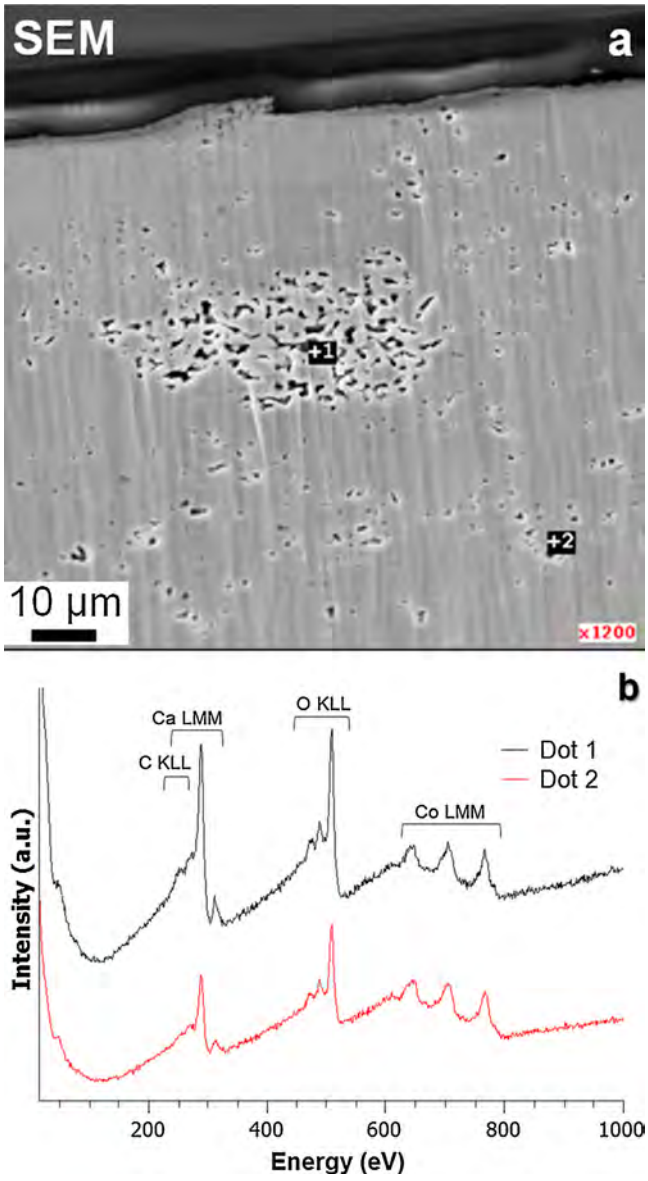

Fig. 4. Auger analyses of two target dots in the undoped material: (a) SEM image with the location of the two dots and (b) the corresponding Auger spectra.

3.4. Thermoelectric properties

Evolution of electrical resistivity with temperature is displayed in Fig. 6a, with the estimated error (4%) [49]. The samples show semiconducting-like behaviour ($d\rho/dT \leq 0$), with lower resistivity values for the Sr-doped samples, in agreement with previous studies [21]. The minimum resistivity values at 800 °C (6.5mΩ cm), are close to those obtained for textured materials prepared through SPS (6mΩ cm) [50], or edge-free SPS (7mΩ cm) [51], and lower than in hot-pressed or sintered specimens (25 and 15mΩ cm, respectively) [14,21]. Several factors may be responsible for high electrical performance, as high density and minor impurities content (only Sr and Ca carbonates have been observed at the surfaces), relatively high Co valence, significant grain alignment, and good electrical connectivity between grains.

Fig. 6a also shows the variation of Seebeck coefficient with temperature in both type of samples, and corresponding error (4%) [49]. The values are positive in the whole measured temperature range, confirming a dominant p-type electronic conduction mechanism. The values of Seebeck coefficient increase with temperature, while being

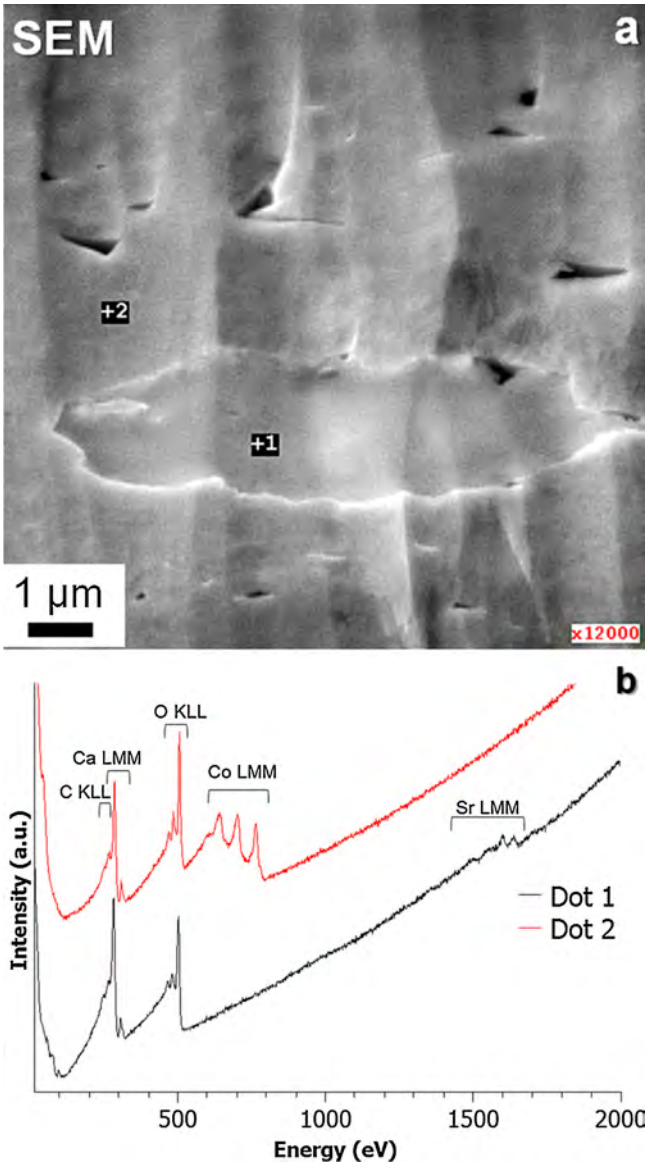

Fig. 5. Auger analyses of two target dots in the Sr-doped material: (a) SEM image showing a Sr-inclusion and the location of the two target dots and (b) the corresponding Auger spectra.

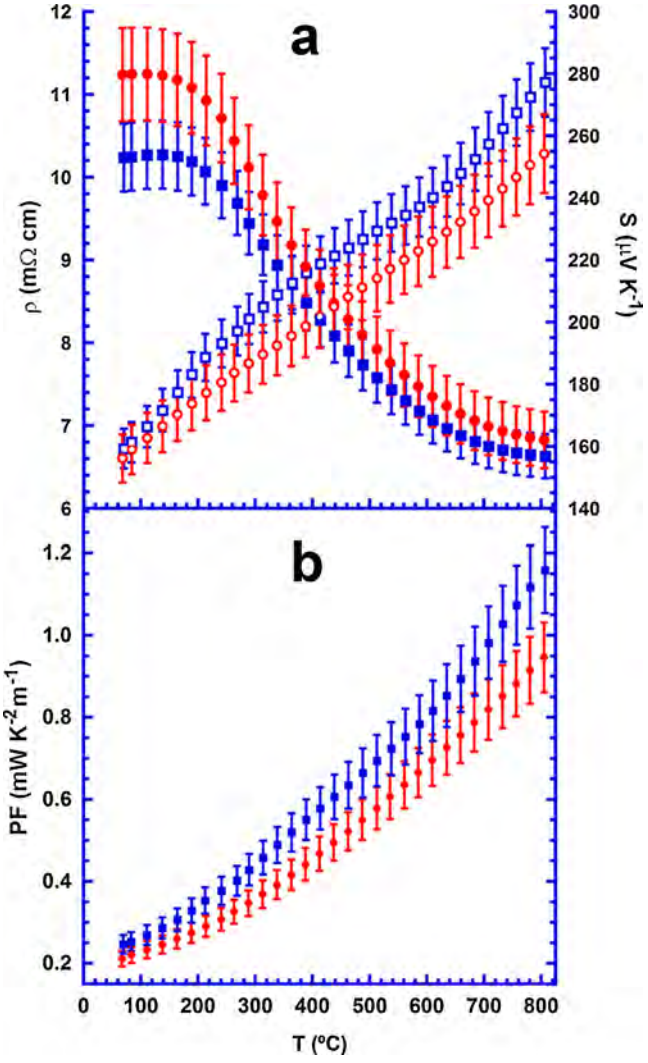

Fig. 6. a) Temperature dependence of the electrical resistivity (filled symbols) and Seebeck coefficient (empty symbols) for the undoped (●, ○); and Sr-doped (■, □) $Ca_3Co_4O_9$ samples, together with their errors; b) Temperature dependence of the power factor for the undoped (●); and Sr-doped (■) $Ca_3Co_4O_9$ samples, together with their error.

notably higher for the Sr-doped material, especially at high temperatures. The data at nearly room temperature suggest similar concentration of charge carriers, in agreement with Koshibae's expression [52]; the same conclusion follows from the oxidation state extracted in XPS analyses ($Co^{+3.3}$). At room temperature (RT), the measured value (150μV/K) is much lower than the predicted by Koshibae's expression (200 μV/K) [53], typical trend observed in previous works on $Ca_3Co_4O_9$ [54,55]. The slight difference found in RT values indicates that Sr addition softly affects the $Ca_3Co_4O_9$ conduction band [56]. The maximum S values at 800 °C (275μV/K) are much higher than the usual values reported in the literature for textured materials produced through SPS (165μV/K) [50], or classically sintered compounds (220μV/K) [21]. It seems counterintuitive, due to the isovalent nature of the substitution and similar average cobalt oxidation state, at least at RT as confirmed by XPS. A weaker increase was observed in $[(Sr_{1-x}Ca_x)_2(O,OH)_2]_q[CoO_2]$, attributed to the effect of changes in misfit parameter [57]. Results for $Ca_{3-x}Sr_xCo_4O_9$ single crystals also suggest higher S in Sr-containing materials, due to the negative chemical pressure effects [58].

The temperature dependence of PF is presented in Fig. 6b, together with its estimated error (9%). PF increases with temperature reaching the highest values reported so far, in the best of our knowledge, for $Ca_3Co_4O_9$ polycrystalline materials. This is mostly provided by very high Seebeck coefficient, as discussed above. Sr-substitution further improves PF values up to 20% in the whole measured temperature range. The highest values at 800 °C (1.16 mW/K^{2}m) are nearly three times higher than the best ones reported in the literature for materials produced via different techniques (0.43 mW/K^{2}m) [25,40,51].

Thermal conductivity has been evaluated at 25–160 °C using photothermal radiometry technique (PTR). Fig. SI4 depicts the temperature dependence of thermal effusivity and diffusivity, showing that Sr-doping decreases both parameters and, consequently, thermal conductivity, presented in Fig. 7a, together with its error (5%) [49]. This result clearly indicates that Sr-doping provides larger contribution to suppress the lattice thermal conductivity if taking into account the corresponding increase in its electronic counterpart. Another contribution to suppressing the lattice thermal conductivity is expected from the different ionic radius of Ca^{2+} and Sr^{2+} cations, which determines the magnitude of the lattice misfit and affects the dynamics of interference between CoO_2 and rock-salt layers [59]. For both

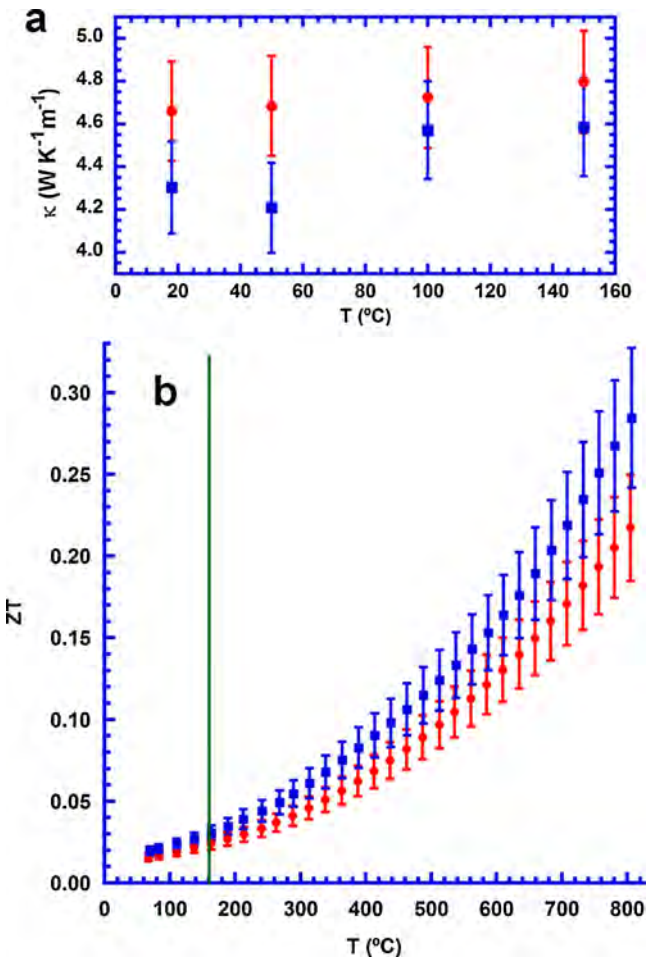

Fig. 7. a)Temperature dependence of thermal conductivity for undoped (●); and Sr-doped (■) samples, together with their errors; and b) Temperature dependence of ZT for undoped (●); and Sr-doped (■) samples, together with their error. The vertical line is a guide for eyes to separate the calculated (low temperatures) and estimated values (high temperatures), considering thermal conductivity constant in the whole temperature range.

materials, thermal conductivity stays roughly constant in the range of studied temperatures (about 4.7, and 4.4 W/K m, for undoped, and Sr-doped samples, respectively).

Based on these thermal conductivity values, ZT, calculated from RT to 160 °C, and estimated for higher temperatures, are shown in Fig. 7b, together with their error (15%) [49]. Sr-doping clearly improved the performances of samples (close to 50% at 800 °C), when compared to the undoped $Ca_3Co_4O_9$. On the other hand, in spite of the impressive improvements achieved in electrical performance, the unusually high thermal conductivities led to lower ZT values than expected. The maximum values at 800 °C (0.29) in the Sr-doped samples are slightly lower than for those prepared using a transient liquid phase (0.35) [60]. On the contrary, at 600 °C, their ZT (0.16) is significantly higher than for textured materials (0.07) [14,30]. Once again, it is necessary to note that the high temperature ZT values are most probably underestimated due to the assumption of a constant thermal conductivity value above 160 °C.

It is clear that this procedure leads to very attractive electrical properties in $Ca_3Co_4O_9$-based materials, decreasing thermal conductivity by Sr substitution. Such simultaneous improvement represents a significant advance, achieved in the present work by combined effects of substitution and processing. This is a very promising result for materials composed of micrometer-sized grains, as such independent tunning of all thermoelectric parameters has been mostly achieved in nanostructured materials. It seems evident that increasing ZT values can be promoted by rare earth elements doping, decreasing thermal conductivity, without significant modification of electrical properties.

4. Conclusions

This work demonstrates how highly-performing $Ca_3Co_4O_9$ thermoelectric materials can be produced through a modified hot-pressing process combined with doping. Microstructural studies showed significant grain orientation, relatively large grain sizes, and low porosity. Density confirmed the low porosity of samples (around 95% of theoretical). XPS analysis has demonstrated that Sr does not modify the $Ca_3Co_4O_9$ valence band, while Auger spectroscopy showed that it enhances the reactivity with moisture, forming Sr and Ca carbonates, especially close to the porosity. Thermoelectric properties are significantly improved by Sr-doping, provided by lower electrical resistivity and thermal conductivity, and higher Seebeck coefficient, compared to the undoped samples. PF of Sr-containing samples was found to be the highest reported so far in this system, mostly due to an unusual enhancement in Seebeck coefficient. In spite of the great improvement of PF, ZT values are only around the best reported in the literature (around 0.29), due to their high thermal conductivity.

Authors contribution

All authors have equally contributed to the article.

Acknowledgements

M. A. Torres, M. A. Madre, J. C. Diez, and A. Sotelo thank the Spanish MINECO-FEDER (MAT2017-82183-C3-1-R) and Gobierno de Aragón-FEDER (Research group T54-17R), for financial support. Authors acknowledge the use of Servicio General de Apoyo a la Investigación-SAI, Universidad de Zaragoza. N.M. Ferreira, A.V. Kovalevsky and F.M. Costa acknowledge the i3N (UID/CTM/50025/2013), CICECO-Aveiro Institute of Materials (UID/CTM/50011/2013) and POCI-01-0145-FEDER-031875 project financed by COMPETE 2020 Program, FCT/MEC and FEDER, POCI in its FEDER/FNR component, under the PT2020 Partnership Agreement. The support from FCT (Portugal) grants SFRH/BPD/111460/2015 and IF/00302/2012, are also acknowledged. Sh. Rasekh acknowledges a FCT grant (SFRH/BPD/124238/2016).

Appendix A. Supplementary data

Supplementary material related to this article can be found, in the online version, at doi:https://doi.org/10.1016/j.jeurceramsoc.2018.12.049.

References

[1] D.M. Rowe (Ed.), Thermoelectrics Handbook: Macro to Nano, CRC press, Boca Raton, FL, 2005.
[2] G. Mahan, B. Sales, J. Sharp, Thermoelectric materials: new approaches to an old problem, Phys. Today 50 (1997) 42–47.
[3] H. Naito, Y. Kohsaka, D. Cooke, H. Arashi, Development of a solar receiver for a high-efficiency thermionic/thermoelectric conversion system, Sol. Energy 58 (1996) 191–195.
[4] C.M. Kim, Y.J. Hwang, Y.H. Ryu, US Patent US6393842. May, 2002.
[5] H. Wang, J. Hwang, M.L. Snedaker, I.-H. Kim, C. Kang, J. Kim, G.D. Stucky, J. Bowers, W. Kim, High thermoelectric performance of a heterogeneous PbTe nanocomposite, Chem. Mater. 27 (2015) 944–949.
[6] J.A. Santamaria, J. Alkorta, J.G. Sevillano, Microcompression tests of single-crystalline and ultrafine grain Bi_2Te_3 thermoelectric material, J. Mater. Res. 30 (2015) 2593–2604.
[7] I. Terasaki, Y. Sasago, K. Uchinokura, Large thermoelectric power in $NaCo_2O_4$ single crystals, Phys. Rev. B 56 (1997) 12685–12687.
[8] F. Kahraman, M.A. Madre, Sh. Rasekh, C. Salvador, P. Bosque, M.A. Torres, J.C. Diez, A. Sotelo, Enhancement of mechanical and thermoelectric properties of $Ca_3Co_4O_9$by Ag addition, J. Eur. Ceram. Soc. 35 (2015) 3835–3841.

[9] K. Miyazawa, F. Amaral, A.V. Kovalevsky, M.P.F. Graca, Hybrid microwave processing of $Ca_3Co_4O_9$ thermoelectrics, Ceram. Int. 42 (2016) 9482–9487.
[10] F. Delorme, C.F. Martin, P. Marudhachalam, G. Guzman, D.O. Ovono, O. Fraboulet, Synthesis of thermoelectric $Ca_3Co_4O_9$ ceramics with high ZT values from a $Co^{II}Co^{III}$-Layered Double Hydroxide precursor, Mater. Res. Bull. 47 (2012) 3287–3291.
[11] R. Funahashi, I. Matsubara, H. Ikuta, T. Takeuchi, U. Mizutani, S. Sodeoka, An oxide single crystal with high thermoelectric performance in air, J. Appl. Phys. 39 (2000) L1127–L1129.
[12] Y. Zhang, J. Zhang, Q. Lu, Synthesis of highly textured $Ca_3Co_4O_9$ ceramics by spark plasma sintering, Ceram. Int. 33 (2007) 1305–1308.
[13] J.G. Noudem, D. Kenfaui, D. Chateigner, M. Gomina, Granular and lamellar thermoelectric oxides consolidated by spark plasma sintering, J. Korean Inst. Electr. Electron. Mater. Eng. 40 (2011) 1100–1106.
[14] H. Wang, X. Sun, X. Yan, D. Huo, X. Li, J.-G. Li, X. Ding, Fabrication and thermoelectric properties of highly textured $Ca_9Co_{12}O_{28}$ ceramic, J. Alloys Compd. 582 (2014) 294–298.
[15] H. Itahara, C. Xia, J. Sugiyama, T. Tani, Fabrication of textured thermoelectric layered cobaltites with various rock salt-type layers by using β-$Co(OH)_2$ platelets as reactive templates, J. Mater. Chem. 14 (2004) 61–66.
[16] Sh. Rasekh, G. Constantinescu, M.A. Torres, M.A. Madre, J.C. Diez, A. Sotelo, Growth rate effect on microstructure and thermoelectric properties of melt grown $Bi_2Ba_2Co_2O_x$ textured ceramics, Adv. Appl. Ceram. 111 (2012) 490–494.
[17] N.M. Ferreira, Sh. Rasekh, F.M. Costa, M.A. Madre, A. Sotelo, J.C. Diez, M.A. Torres, New method to improve the grain alignment and performance of thermoelectric ceramics, Mater. Lett. 83 (2012) 144–147.
[18] X.Y. Song, Y. Chen, S. Chen, E. Barbero, E.L. Thomas, P. Barnes, Significant enhancement of electrical transport properties of thermoelectric $Ca_3Co_4O_{9+\delta}$ through Yb doping, Solid State Commun. 152 (2012) 1509–1512.
[19] H. Liu, G.C. Lin, X.D. Ding, J.X. Zhang, Mechanical relaxation in thermoelectric oxide $Ca_{3-x}Sr_xCo_4O_{9+\delta}$ ($x=0$, 0.25, 0.5, 1.0) associated with oxygen vacancies, J. Solid State Chem. 200 (2013) 305–309.
[20] G. Kirat, M.A. Aksan, Sh. Rasekh, M.A. Madre, J.C. Diez, A. Sotelo, Decrease of $Ca_3Co_4O_{9+\delta}$ thermal conductivity by Yb-doping, Ceram. Int. 41 (2015) 12529–12534.
[21] G. Constantinescu, Sh. Rasekh, M.A. Torres, J.C. Diez, M.A. Madre, A. Sotelo, Effect of Sr substitution for Ca on the $Ca_3Co_4O_9$ thermoelectric properties, J. Alloys Compd. 577 (2013) 511–515.
[22] F. Delorme, C. Fernandez Martin, P. Marudhachalam, D. Ovono Ovono, G. Guzman, Effect of Ca substitution by Sr on the thermoelectric properties of $Ca_3Co_4O_9$ ceramics, J. Alloys Compd. 509 (2011) 2311–2315.
[23] S. Li, R. Funahashi, I. Matsubara, H. Yamada, K. Ueno, S. Sodeoka, Synthesis and thermoelectric properties of the new oxide ceramics $Ca_{3-x}Sr_xCo_4O_{9+\delta}$ ($x=0.0$–1.0), Ceram. Int. 27 (2001) 321–324.
[24] L.B. Wang, A. Maignan, D. Pelloquin, S. Hebert, B. Raveau, Transport and magnetic properties of $Ca_{3-x}Sr_xCo_4O_9$, J. Appl. Phys. 92 (2002) 124–128.
[25] A. Sotelo, Sh. Rasekh, M.A. Torres, P. Bosque, M.A. Madre, J.C. Diez, Effect of synthesis methods on the $Ca_3Co_4O_9$ thermoelectric ceramic performances, J. Solid State Chem. 221 (2015) 247–254.
[26] D. Flahaut, J. Allouche, A. Sotelo, Sh. Rasekh, M.A. Torres, M.A. Madre, J.C. Diez, Role of Ag in textured-annealed $Bi_2Ca_2Co_{1.7}O_x$ thermoelectric ceramic, Acta Mater. 102 (2016) 273–283.
[27] P.E. Nordal, S.O. Kanstad, Photothermal radiometry, Phys. Scr. 20 (1979) 659–662.
[28] M. Depriester, P. Hus, S. Delenclos, A.H. Sahraoui, New methodology for thermal parameter measurements in solids using photothermal radiometry, Rev. Sci. Instr. 76 (2005) 074902.
[29] N. Prasoetsopha, S. Pinitsoontorn, T. Kamwanna, V. Amornkitbamrung, K. Kurosaki, Y. Ohishi, H. Muta, S. Yamanaka, The effect of Cr substitution on the structure and properties of misfit-layered $Ca_3Co_{4-x}Cr_xO_{9+\delta}$ thermoelectric oxides, J. Alloys Compd. 588 (2014) 199–205.
[30] D. Kenfaui, B. Lenoir, D. Chateigner, B. Ouladdiaf, M. Gomina, J.G. Noudem, Development of multilayer textured $Ca_3Co_4O_9$ materials for thermoelectric generators: influence of the anisotropy on the transport properties, J. Eur. Ceram. Soc. 32 (2012) 2405–2414.
[31] Y. Miyazaki, M. Onoda, T. Oku, M. Kikuchi, Y. Ishii, Y. Ono, Y. Morii, T. Kajitani, Modulated structure of the thermoelectric compound $[Ca_2CoO_3]_{0.62}CoO_2$, J. Phys. Soc. Jpn. 71 (2002) 491–497.
[32] E. Woermann, A. Muan, Phase equilibria in the system CaO–cobalt oxide in air, J. Inorg. Nucl. Chem. 32 (1970) 1455–1459.
[33] C.H. Hervoches, H. Okamoto, A. Kjekshus, H. Fjellvag, B.C. Hauback, Crystal structure and magnetic properties of the solid-solution phase $Ca_3Co_{2-v}Mn_vO_6$, J. Solid State Chem. 182 (2009) 331–338.
[34] F. Delorme, P. Diaz-Chao, E. Guilmeau, F. Giovannelli, Thermoelectric properties of $Ca_3Co_4O_9$–Co_3O_4 composites, Ceram. Int. 41 (2015) 10038–10043.
[35] N. Puri, R.P. Tandon, A.K. Mahapatro, Fully dense hot pressed calcium cobalt oxide ceramics, Ceram. Int. 44 (2018) 6337–6342.
[36] A.C. Masset, C. Michel, A. Maignan, M. Hervieu, O. Toulemonde, F. Studer, B. Raveau, J. Hejtmanek, Misfit-layered cobaltite with an anisotropic giant magnetoresistance: $Ca_3Co_4O_9$, Phys. Rev. B 62 (2000) 166–175.
[37] D. Sedmidubsky, V. Jakes, O. Jankovsky, J. Leitner, Z. Sofer, J. Hejtmanek, Phase equilibria in Ca-Co-O system, J. Solid State Chem. 194 (2012) 199–205.
[38] D. Kenfaui, D. Chateigner, M. Gomina, J.G. Noudem, Texture, mechanical and thermoelectric properties of $Ca_3Co_4O_9$ ceramics, J. Alloys Compd. 490 (2010) 472–479.
[39] M. Bittner, L. Helmich, F. Nietschke, B. Geppert, O. Oeckler, A. Feldhoff, Porous $Ca_3Co_4O_9$ with enhanced thermoelectric properties derived from Sol–Gel synthesis, J. Eur. Ceram. Soc. 37 (2017) 3909–3915.
[40] T. Schulz, J. Topfer, Thermoelectric properties of $Ca_3Co_4O_9$ ceramics prepared by an alternative pressure-less sintering/annealing method, J. Alloys Compd. 659 (2016) 122–126.
[41] M.A. Madre, F.M. Costa, N.M. Ferreira, A. Sotelo, M.A. Torres, G. Constantinescu, Sh. Rasekh, J.C. Diez, Preparation of high-performance $Ca_3Co_4O_9$ thermoelectric ceramics produced by a new two-step method, J. Eur. Ceram. Soc. 33 (2013) 1747–1754.
[42] F. Delorme, D. Ovono Ovono, P. Marudhachalam, C. Fernandez Martin, O. Fraboulet, Effect of precursors size on the thermoelectric properties of $Ca_3Co_4O_9$ ceramics, Mater. Res. Bull. 47 (2012) 1169–1175.
[43] L. Daheron, R. Dedryvere, H. Martinez, M. Menetrier, C. Denage, C. Delmas, D. Gonbeau, Electron transfer mechanisms upon lithium deintercalation from $LiCoO_2$ to CoO_2 investigated by XPS, Chem. Mater. 20 (2008) 583–590.
[44] Y. Wakisaka, S. Hirata, T. Mizokawa, Y. Suzuki, Y. Miyazaki, T. Kajitani, Electronic structure of $Ca_3Co_4O_9$ studied by photoemission spectroscopy: phase separation and charge localization, Phys. Rev. B 78 (2008) 235107.
[45] J.-C. Dupin, D. Gonbeau, P. Vinatier, A. Levasseur, Systematic XPS studies of metal oxides, hydroxides and peroxides, Phys. Chem. Chem. Phys. 2 (2000) 1319–1324.
[46] M.I. Sosulnikov, Y.A. Teterin, X-Ray photoelectron studies of Ca, Sr and Ba and their oxides and carbonates, J. Electron. Spectrosc. Relat. Phenom. 59 (1992) 111–126.
[47] A.B. Christie, J. Lee, I. Sutherland, J.M. Walls, An XPS study of ion-induced compositional changes with group-II and group-IV compounds, Appl. Surf. Sci. 15 (1983) 224–237.
[48] R.L. Frost, M.C. Hales, W.N. Martens, Thermogravimetric analysis of selected group (II) carbonate minerals – implication for the geosequestration of greenhouse gas, J. Therm. Anal. Calorim. 95 (2009) 999–1005.
[49] M.A. Madre, F.M. Costa, N.M. Ferreira, S.I.R. Costa, Sh. Rasekh, M.A. Torres, J.C. Diez, V.S. Amaral, J.S. Amaral, A. Sotelo, High thermoelectric performance in $Bi_{2-x}Pb_xBa_2Co_2O_y$ promoted by directional growth and annealing, J. Eur. Ceram. Soc. 36 (2016) 67–74.
[50] N.Y. Wu, T.C. Holgate, N.V. Nong, N. Pryds, S. Linderoth, High temperature thermoelectric properties of $Ca_3Co_4O_{9+\delta}$ by auto-combustion synthesis and spark plasma sintering, J. Eur. Ceram. Soc. 34 (2014) 925–931.
[51] J.G. Noudem, D. Kenfaui, D. Chateigner, M. Gomina, Toward the enhancement of thermoelectric properties of lamellar $Ca_3Co_4O_9$ by edge-free spark plasma texturing, Scr. Mater. 66 (2012) 258–260.
[52] W. Koshibae, K. Tsuitsui, S. Maekawa, Thermopower in cobalt oxides, Phys. Rev. B Condens. Matter. 62 (2000) 6869–6872.
[53] A. Maignan, D. Pelloquin, S. Hebert, Y. Klein, M. Hervieu, Thermoelectric power in misfit cobaltites ceramics: optimization by chemical substitutions, Bol. Soc. Esp. Ceram. V. 45 (2006) 122–125.
[54] M. Karppinen, H. Fjellvag, T. Konno, Y. Morita, T. Motohashi, H. Yamauchi, Evidence for oxygen vacancies in misfit-layered calcium cobalt oxide, $[CoCa_2O_3]_qCoO_2$, Chem. Mater. 16 (2004) 2790–2793.
[55] A. Sotelo, G. Constantinescu, Sh. Rasekh, M.A. Torres, J.C. Diez, M.A. Madre, Improvement of thermoelectric properties of $Ca_3Co_4O_9$ using soft chemistry synthetic methods, J. Eur. Ceram. Soc. 32 (2012) 2415–2422.
[56] Sh. Rasekh, M.A. Torres, G. Constantinescu, M.A. Madre, J.C. Diez, A. Sotelo, Effect of Cu by Co substitution on $Ca_3Co_4O_9$ thermoelectric ceramics, J. Mater. Sci. Mater. Electron. 24 (2013) 2309–2314.
[57] H. Yamauchi, L. Karvonen, T. Egashira, Y. Tanaka, M. Karppinen, Ca-for-Sr substitution in the thermoelectric $[(Sr,Ca)_2(O,OH)_2]_q[CoO_2]$ misfit-layered cobaltoxide system, J. Solid State Chem. 184 (2011) 64–69.
[58] K. Saito, R. Okazaki, Electron correlation effect in the thermoelectric oxide $Ca_{3-x}Sr_xCo_4O_9$ single crystals, J. Appl. Phys. 56 (2017) 043201.
[59] S. Fujii, M. Yoshiya, Manipulating thermal conductivity by interfacial modification of misfit-layered cobaltites $Ca_3Co_4O_9$, J. Korean Inst. Electr. Electron. Mater. Eng. 45 (2016) 1217–1226.
[60] A. Sotelo, F.M. Costa, N.M. Ferreira, A. Kovalevsky, M.C. Ferro, V.S. Amaral, J.S. Amaral, Sh. Rasekh, M.A. Torres, M.A. Madre, J.C. Diez, Tailoring $Ca_3Co_4O_9$ microstructure and performances using a transient liquid phase sintering additive, J. Eur. Ceram. Soc. 36 (2016) 1025–1032.